Measurement 195 (2022) 111112

Contents lists available at ScienceDirect

Measurement

journal homepage: www.elsevier.com/locate/measurement

Robot assisted electrical impedance scanning for tissue bioimpedance spectroscopy measurement

Zhuoqi Cheng [a], Diego Dall'Alba [b,*], Kim Lindberg Schwaner [a], Paolo Fiorini [b], Thiusius Rajeeth Savarimuthu [a]

[a] Mærsk Mc Kinney Møller Institute, University of Southern Denmark, 5230 Odense, Denmark
[b] Department of Computer Science, University of Verona, 37134 Verona, Italy

ARTICLE INFO

Keywords:
Bioimpedance Spectroscopy
Tri-polar sensing configuration
Tissue identification
Electrodes position control
Robot-Assisted Minimally Invasive Surgery

ABSTRACT

Intraoperative tissue identification is important and frequently required in modern surgical approaches for guiding operation. For this purpose, a novel robot assisted sensing system equipped with a wide-band impedance spectroscope is developed. Without introducing an external sensor probe to the operating site, the proposed system incorporates two robotic instruments for electric current excitation and voltage measurement. Based on the developed measurement strategy and algorithm, the electrical conductivity and permittivity of the tissue region can be calculated. Experiments based on simulation, salines and ex-vivo tissue phantoms are conducted. The experimental results demonstrate that the proposed system has a high measurement accuracy (≥97%). Through a simple support vector machine, a 100% accuracy is achieved for identifying five different tissues. Given the convincing results, the presented sensing system shows great potential in offering effective, fast, and safe tissue inspection.

1. Introduction

Robot-Assisted Minimally Invasive Surgery (RAMIS) has been widely adopted in modern medical systems. In RAMIS, surgeons control robotic instruments to access the patient's body cavity via small incisions and perform the surgery. Thanks to the enhanced precision and dexterity provided by robotic systems, surgeons can conveniently perform procedures that would be difficult using conventional laparoscopic technique [1]. RAMIS is reported to have several patient-related benefits, such as less pain and scarring, shorter hospital stays, and lower postoperative morbidity [2].

The introduction of novel technical features is essential to further extend the use of RAMIS systems to increasingly complex procedures and continue improving the postoperative outcome. The most requested technical features are related to the improvement of surgical instruments and the introduction of Advanced Intraoperative Sensing (AIS) methods [3]. An ideal AIS method should improve the localization of areas that are difficult to recognize with other intraoperative sensing modalities with minimal interruption of the surgical workflow. AIS technology is fundamental to improve surgeons' performance in tissue discrimination and manipulation. Additionally, AIS can support the introduction of increasingly automated systems that will pave the way for autonomous surgical systems in the future.

The evolution of surgical robotics has been trending towards a higher level of automation across an increasingly broad range of surgical procedures, from diagnosis to treatment [4]. Automating surgery can potentially increase and ensure consistent procedure quality while reducing the surgeons' workload. In turn, this can increase hospital throughput and make advanced surgical procedures available to an increased number of patients. AIS technologies are required to enhance surgical robots for more complicated procedures and gradually improve their decision support capabilities, following the cognitive surgical robot concept of [5]. Thus, perceiving the surgical environment automatically and accurately becomes critical and essential for the new generation of surgical robots.

In this study, we present a Robot-Assisted Electrical Impedance Scanning (RAEIS) spectroscopy measurement system. The system introduces an additional AIS modality to surgical robots and enables automatically and quickly identifying different tissue types. Compared with our previous works [6,7], we improve the RAEIS system's performance by applying spectroscopy measurements and optimizing the acquisition protocol, focusing on electrode placement.

Most clinically available RAMIS systems are equipped with very limited real-time AIS, mainly based on a stereoscopic endoscopic camera

* Corresponding author.
E-mail addresses: zch@sdu.dk (Z. Cheng), diego.dallalba@univr.it (D. Dall'Alba), kls@sdu.dk (K.L. Schwaner), paolo.fiorini@univr.it (P. Fiorini), trs@sdu.dk (T.R. Savarimuthu).

https://doi.org/10.1016/j.measurement.2022.111112
Received 7 June 2021; Received in revised form 24 March 2022; Accepted 26 March 2022
Available online 4 April 2022

that facilitates depth perception. For instance, existing surgical robots do not provide surgeons with haptic feedback, which is an advantage of conventional open access surgery [8]. Through palpating the tissue, surgeons can locate a pathological region that is generally harder than the surrounding healthy tissue. This unfulfilled requirement has motivated many previous engineering developments to restore the missing haptic perception to the robots [9]. In addition to integrating force-sensing directly on the forceps [10], additional tools that can assist the palpation have been developed [11,12]. These force perception technologies require significant changes to surgical instruments or the clinical protocol. In turn, this can make the certification and adoption process complex and slow. The RAEIS system proposed in this work, on the other hand, requires minimal changes to the surgical instruments and to the workflow of RAMIS interventions.

Various alternative AIS technologies have been developed to compensate for the lack of haptic sensation. A popular one is fluorescence technology which can effectively enhance the visualization of dye-marked tissues such as blood vessels. This technology requires injection of a contrast medium before or during a procedure. The proposed method does not require the use of a contrast agent.

Researchers have also reported the use of a drop-in ultrasound transducer (X12C4, BK Medical) to improve surgical outcomes and margin rates in robotic-assisted renal partial nephrectomy [13]. The drop-in ultrasound transducer is grasped by a robotic forceps to scan and detect hidden cancerous tissues. Ultrasound scanning is done manually by the surgeon and requires specific skills to be correctly performed and interpreted. In our work, the data acquisition procedure is completely automated, requiring the surgeon only to select a point of interest and a scanning direction. It is worth noting that the above-mentioned technologies aim to visualize a specific tissue from the background instead of indicating the specific tissue type and/or the tissue's pathological status, as in the proposed system.

In recent years, bio-impedance spectroscopy has been of increasing interest in cell biology and biotechnology [14]. Specifically, the frequency response of electrical bioimpedance (EBI) has been exploited for estimating tissue types. Previous studies have reported that different tissues have significantly different electrical characteristics, and even for the same tissue types, the differences of EBI characteristics can reflect their healthy and pathological status [15–17]. Accurate tissue classification based on the electrical property has been demonstrated in [18].

According to previous studies [19–21], cancerous tissue in the prostate, colorectal region, and thyroid generally contains higher salinity and water when compared to benign stroma and glandular tissue. This is reflected by significantly lower conductivity at frequencies between 0.1 and 100 kHz and significantly higher permittivity at 100 kHz. By taking advantage of tissues' EBI characteristics, several devices, such as ZedScan (Zilico Ltd., UK) and Nevisense (Scibase AB., Norway), have been developed and are available in the market. So far, few EBI probes have been designed for assisting during RAMIS [17,22]. The maximum diameter of RAMIS access ports, i.e., 12 mm, constrains the size of EBI probes, limiting the design space for the number and orientation of the electrodes. Hence, these probes commonly have concentrated sensitivity, hardly improving the signal-noise ratio of the measurement.

Electrical Impedance Tomography (EIT) is another well-known technology for visualizing tissues' electrical properties. This technology has been used in a variety of medical applications such as prostate and breast cancer detection [17,23,24]. Generally, the reconstructed EIT image is used for showing the contrast of conductivity within a region rather than sensing the spectroscopic response in a specific tissue region. The previous art of EIT has been made a miniaturized probe for imaging cancer margin [17]. However, integrating a sensor probe to RAMIS requires good manipulation skills. Also, a limited range can be sensed due to the size constraint.

A previous study has proposed to use the existing instruments of a medical robotic system for the EBI sensing on tissue surface and offer the visualization of the impedance distribution through augmented reality [25]. Such a EBI sensing technology can assist in the localization of pathological tissue automatically, promoting the autonomy level of future surgical robotic systems. However, the previous setups use a bipolar sensing configuration, whose reliability highly depends on the contacting area between the electrodes and the tissue. Due to the soft tissue deformation, the control of electrodes pressing depth on the tissue is normally difficult. This yields relatively big variation, making it hard to improve tissue identification accuracy.

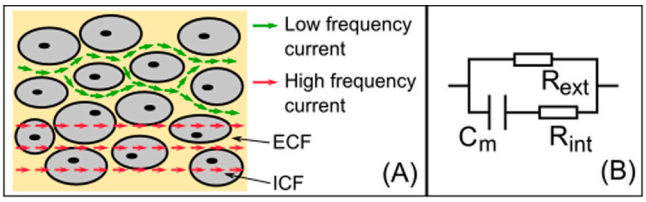

Fig. 1. (A) Modeling the alternating electrical current passing through tissue; (B) The Cole model representing the electrical characteristics of biological tissues.

To summarize, the proposed RAEIS system is easy to implement on currently existing surgical robot systems and follows the current operational workflow. Compared to the other existing AIS technologies, the proposed system can improve the surgical robotic system capability in identifying different tissues, integrating and complementing other AIS already used and previously described in this section. To the best of our knowledge, this paper presents the first robot assisted sensing system for wide spectrum measurements of tissues' conductivity and permittivity intraoperatively. Compared to the previous works in literature, this research exploits the flexibility of the robotic technology resulting to the improvement of acquisition process and sensing reliability. The detailed contributions of this paper are summarized as follows.

- Development of a method for wide-band impedance spectroscopic measurement and an algorithm to compute tissue conductivity and permittivity.
- Hardware realization and control strategy for a reliable and noise resistant tri-polar sensing setup.
- Enhanced measurement accuracy by optimizing electrode positioning in the measurement protocol.

The rest of the paper is organized as follows. After the introduction in Section 1, Section 2 introduces the methodology and the modeling. In Section 3, a series of experiments are designed and performed to evaluate the system. The experiments include a Finite Element Simulation study, an experiment based on a saline tank, and an experiment based on ex vivo tissue samples. Sections 4 and 5 presents and discusses the results. Section 6 concludes this paper.

2. Materials and methods

2.1. Bioimpedance spectroscopy measurement

The microscopic electrical model of biological tissue is shown in Fig. 1(A). The intracellular fluid (ICF) is the cytosol enclosed in cells by their plasma membranes. Extracellular fluid (ECF) surrounds the cells and serves as a circulating reservoir. To describe the electrical property of biological tissue, the Cole model as shown in Fig. 1(B) is commonly used [26]. The equivalent circuit comprises a capacitor C_m representing the outer lipid membrane, and two resistors R_{int} and R_{ext} representing the intracellular volume and extracellular volume, respectively.

Since the dielectric/conductive property of biological tissue is frequency dependent, the measurement is conducted by the response to the flow of an applied alternating electrical current with given amplitude and frequency. Considering that the intact cell membranes are generally unchangeable, low frequency current predominantly flow

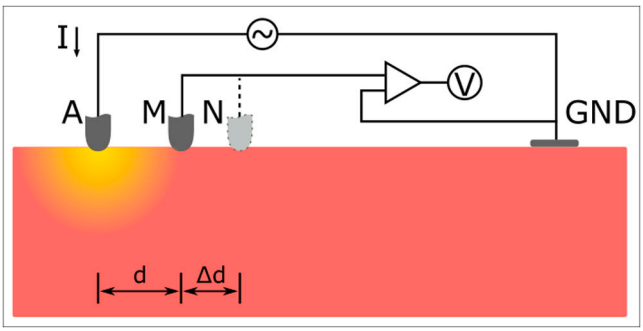

Fig. 2. Modeling the tri-polar EBI measurement including an electrode for current injection (electrode at position A), an electrode for voltage measurement at position M, and a ground electrode indicated as GND.

around the cells [14,27]. Only at higher frequencies, the impedance decreases owing to the accessibility of the cytoplasm as current path. The most commonly used frequency range is from 1 kHz to 1 MHz which is also known as the β-dispersion. The Cole model indicates that excitation under different frequencies leads to different impedance information of the tissue.

In addition, it is more accurate and preferable to describe the electrical characteristics of biological tissue using conductivity and permittivity, instead of the probe dependent impedance module and phrase angle. To derive the conductivity and permittivity based on the measured complex impedance, the sensing system needs to be either calibrated with known media or given knowledge related to the electrodes configuration. This research uses the latter method and more technical details are provided as follows.

2.2. Tri-polar electrical bioimpedance spectroscopy

This study is based on the measurement method presented in [6]. The RAEIS exploits a tri-polar EBI sensing configuration with three electrodes: one current source electrode (CSE), one voltage measurement electrode (VME), and one ground electrode (GND). The GND electrode should be relatively large and attached to a remote site of the measured object. Compared to a bi-polar configuration [28], a tri-polar configuration can improve the measurement accuracy by compensating for the contact impedance at the CSE through a controlled current source [29], and getting rid of electrode polarization at the VME [27].

The tri-polar sensing method can be modeled as shown in Fig. 2. Excitation current I is injected to the material under test (MUT) via the CSE at position A. According to [6], the sensitivity in the detection of subsurface heterogeneous region can be small when its depth is greater than half of the distance between CSE and VME. Given that the electrodes distance is set relatively small in this study, we assume that the material of this small region around A is homogeneous. In this case, the current flow disperses from the source radially into the MUT. Considering that the current distribution is uniform over a hemispherical shell centered at A, the current density at point M is given by

$$J_M = \frac{I}{2\pi d^2} \tag{1}$$

where d denotes the distance of $|AM|$. Since biological material is considered as a dielectrics, this study treats its frequency-dependent electrical property as a model of complex conductivity $\hat{\sigma}$ (as described in Chapter 3 of [14]), which is given as

$$\hat{\sigma} = \sigma - j\omega\epsilon_0\epsilon_r \tag{2}$$

where ω is the excitation frequency $2\pi f$. According to the Maxwell's equations, the electrical potential at position M can be calculated by integrating Eq. (1) as follows

$$V_M = -\int_{r_0}^{d} \frac{I\partial d}{2\pi\hat{\sigma}d^2} = \frac{I}{2\pi\hat{\sigma}}\left(\frac{1}{d} - \frac{1}{r_0}\right) \tag{3}$$

During the measurement, the CSE is required to press on the tissue slightly. This causes the soft tissue deformation surrounding the tip of the CSE. The parameter r_0 in Eq. (3) represents the equivalent radius of the CSE tip which is immersed in the tissue.

It is generally hard to measure or control the value r_0. Therefore, we choose to use the potential difference to remove its impact. Considering that the potentials of two positions on the tissue surface M and N are measured, the electrical potential difference is

$$V_{MN} = \frac{I}{2\pi}\left(\frac{1}{d} - \frac{1}{d+\Delta d}\right)\frac{1}{\hat{\sigma}} \tag{4}$$

Using Eq. (4) for computation can effectively get rid of the uncertainty due to the electrode-tissue contact of the CSE.

For brevity, we use κ to denote the factor related to the measurement setting:

$$\kappa = \frac{1}{d} - \frac{1}{d+\Delta d} \tag{5}$$

Subsequently, the relationship between the measured impedance difference Z_{MN} and the electrical property of the MUT can be written as

$$Z_{MN} = \frac{V_{MN}}{I} = \frac{\kappa}{2\pi\hat{\sigma}} \tag{6}$$

The impedance measurement Z_{MN} includes a real component and an imaginary component, namely $Z_{MN} = Re_{MN} + jIm_{MN}$. Furthermore, we can calculate the conductivity σ and relative permittivity ε of the MUT by substituting Eq. (2) into Eq. (6):

$$\sigma = \frac{\kappa}{2\pi}\frac{Re_{MN}}{Re_{MN}^2 + Im_{MN}^2} \tag{7}$$

$$\varepsilon_r = \frac{\kappa}{4\pi^2 f\epsilon_0}\frac{Im_{MN}}{Re_{MN}^2 + Im_{MN}^2} \tag{8}$$

To improve the measurement accuracy, the voltage measurements are conducted on multiple positions at different distances d to the CSE. We use $\sigma(d_i)$ and $\varepsilon(d_i)$ to denote the measured conductivity and permittivity which are measured at d_i. A weighted average is implemented to represent the electrical property of the MUT.

$$\bar{\sigma} = \frac{\sum(w_i\sigma(d_i))}{\sum w_i} \tag{9}$$

$$\bar{\varepsilon}_r = \frac{\sum(w_i\varepsilon_r(d_i))}{\sum w_i} \tag{10}$$

We propose to design the weights w_i in such a way that the region close to the CSE has a relatively higher contribution to the measurement results. Also, the weight decreases gradually for the measurement further from the CSE. This is because a smaller d_i corresponds to the measurements of the smaller region centered at the CSE according to Eq. (3). In this study, we set the weight w_i equal to the reciprocal of d_i.

$$w_i = \frac{1}{d_i} \tag{11}$$

Both $\bar{\sigma}$ and $\bar{\varepsilon}_r$ are acquired as a function of different frequencies f. For a tissue identification task, a vector can be defined containing the values of $\bar{\sigma}$ and $\bar{\varepsilon}_r$ at different frequencies. These data can be used for training a machine learning classifier.

2.3. System setup and calibration

The proposed EBI spectroscopic measurement method requires the collaboration of two surgical instruments as electrodes. Specifically, one of the instruments is used as the CSE and the other one is acted as

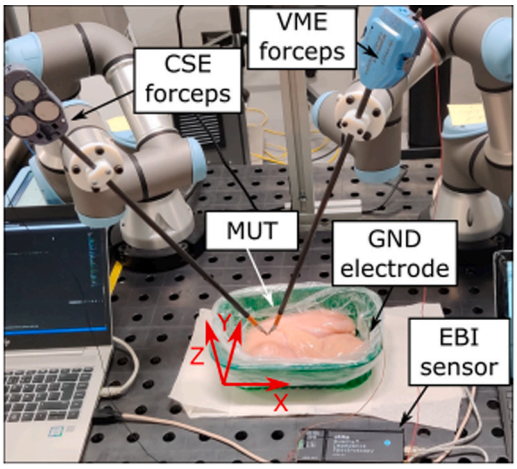

Fig. 3. The setup of the RAEIS system.

the VME. These instruments can be already available electrosurgery instruments used for cautery or tissue dissection. Fig. 3 shows an example setup where two da Vinci robotic scissors (Intuitive Surgical Inc., USA) are used as electrodes. The selected scissors are normally used for electrosurgery, thus they can naturally serve as a monopolar electrode. As shown in Fig. 5(C), the scissors are controlled to press slightly onto the tissue to avoid tissue damage while ensuring optimal contact between tissue and electrode. Considering the tissue deformation and scissors shape, the actual electrode dimensions can be approximated as a 1 mm cube with round edges. These scissors are mounted on the end of UR3 robotic arms (Universal Robots A/S, Denmark) for position control. For impedance spectroscopic measurement, a spectroscopy device (Quadra, Eliko Tehnoloogia Arenduskeskus, Estonia) is used. This device is able to perform measurements at 15 frequencies simultaneously with a sampling period of 1 ms. Sampling frequencies can range from 1 kHz to 349 kHz. The Quadra has a 99.9% measurement accuracy according to the device datasheet.[1]

Calibration of the system consists of two steps: a kinematic calibration and an electrical calibration. The kinematic calibration aims to register the two robots in the same global frame (the red frame in Fig. 3). It is done as follows. We first define the instrument center point for each robot by fixing the electrode tip at a point and manually driving the robotic arm to different postures. The transformation from the instrument tip to the robot end-effector can be computed automatically via the UR robots' PolyScope software. Then we configure the transformation between the robotic base frame to the global frame. This is done by manually driving the robot to nine reference points in the global frame by the instrument tip. The corresponding robotic coordinates are recorded and used to compute the coordinates transformation. After the calibration, the re-projection error is computed and found to be 0.09 mm and 0.12 mm for the CSE instrument and the VME instrument respectively.

The electrical calibration is carried out to ensure high accuracy for the impedance sensor. The calibration is done by connecting resistors with known values across the CSE and VME instrument. Three resistors of 51 Ω, 100 Ω, and 500 Ω are selected as those values are within the range of tissues, according to [30]. The Root-Mean-Square-Error (RMSE) between the measured resistance and the referenced values at different frequencies are found to all be <0.8 %, and the absolute values of all the measured phase angles are <0.13°. This indicates that the developed system can perform spectroscopic measurements with high accuracy.

[1] https://www.eliko.ee/products/quadra-impedance-spectroscopy.

2.4. Scanning protocol design and parameter optimization

The RAEIS system can be operated in a user-supervised autonomous manner or as a key sensing component in future autonomous surgery. The human robot collaborative strategy is providing the surgeon with high flexibility and convenience for a tissue inspection task at a specific region while the process safety can be assured. Also, reliable tissue recognition is important for environmental exploration and registration when robot takes the role of decision making in surgery.

Taking the surgeon robot collaborative operation as an example, the measurement procedure starts by manually selecting an inspection point on the tissue surface and a scanning direction. The CSE instrument is controlled to reach the inspection point and presses its tip on the site 2 mm downwards to ensure a good contact with the tissue. Then the VME instrument conducts the measurement of electrical potential on 13 positions on the tissue surface along the defined direction autonomously as shown in Fig. 4. The robot controls the VME to $H = 3$ mm above a target point, and then approaches the target point downwards with a relatively small speed (Fig. 4(A)). The contact of tissue can be detected immediately by monitoring a significant decrease of impedance. After the tissue contact is detected, the VME is required to move 2 mm downwards in order to have a reliable contact (Fig. 4(B)). Then EBI spectroscopic measurements are conducted, after which the VME is lifted back to $H = 3$ mm above tissue surface (Fig. 4(C)) and moved above the next measurement point (Fig. 4(D)).

During scanning, d is a key parameter which can impact the measurement accuracy of the proposed system significantly. The lower bound of d is set based on two considerations. First, the two instrument cannot be placed too close for preventing potential collision. Second, there is a potential uncertainty of the contacting point on the VME. As shown in Fig. 5, due to the tissue rupture, deformation or uneven surface, the extreme cases would be the tissue-electrode contacting point is located on the left edge (refer to the upper left subfigure (A)) or the right edge (refer to the upper middle subfigure (B)). Therefore, a sensitivity analysis is performed to estimate the maximum error due to this variance. Given that the width of an ordinary robotic scissors is about 1 mm (please refer to the upper right subfigure (C)), we calculate the maximum error of κ by assuming an offset of ± 0.5 mm for d. Specifically, we assume that the measurement is conducted on a homogeneous material. As indicated by Eq. (6), the measured Z is proportional to κ. Thereby, the measurement error is approximated as the relative error of κ in consideration of the ± 0.5 mm offset. By comparing the κ value based on $d \pm 0.5$ mm and its theoretical value, the maximum error is calculated and plotted in Fig. 5(D). Based on the above two considerations, the lower bound of the d range is decided to be 6 mm which can guarantee that the maximum error due to VME size is smaller than 18%.

In addition, the upper bound of the range for d is set based on the following considerations. Eq. (3) indicates that the measured voltage V_M decreases almost proportionally to the reciprocal of d. Given that the magnitude of the injected current should be controlled within a safe range (for instance, 1 mA according to IEC 60601), the signal magnitude of measurement on materials of relatively high conductivity such as muscle can be weak with d>20 mm and possibly dominated by physiological signal noise. Also, the weights are set as the reciprocal of d in this study. Measurements at the position far away from the CSE have limited contribution to the results.

In this study, we also investigate the use of varying Δd_i for the measurement at different positions of d_i in order to improve the signal-noise ratio. As mentioned above, the electrical potentials on the tissue surface are acquired at multiple positions through VME. The distance at each measurement point relative to the CSE is denoted as d_i, and Δd_i is used to denote $d_{i+1} - d_i$. According to Eq. (6), V_{MN} is proportional to factor κ. Through optimizing the setting of κ, the objective is to ensure that V_{MN} is relatively big and within a bounded range. In this case, the

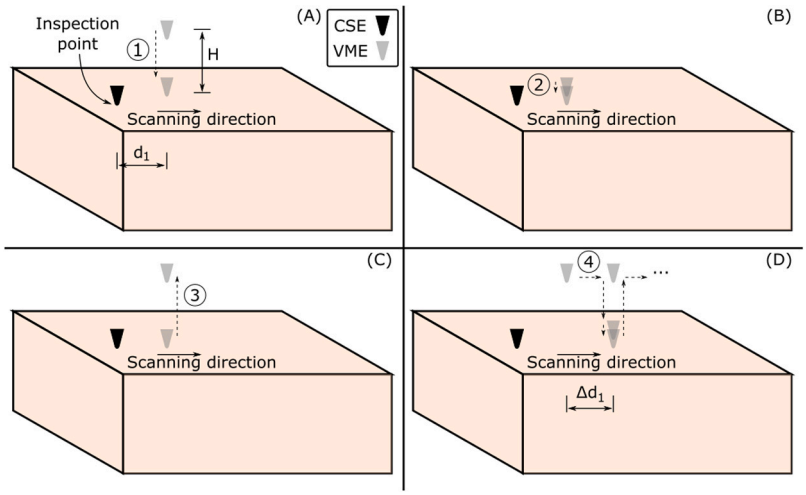

Fig. 4. The scanning process for electrical spectroscopic measurement using the RAEIS system: (A) The robot controls the VME to $H = 3$ mm above a target point, and then approaches the point downwards with a relatively small speed; (B) After the tissue contact is detected, the VME is required to move 2 mm downwards; (C) after the measurement, the VME is lifted $H = 3$ mm; (D) The VME is moved above the next target point. Please see the main text for the definition of d_i and Δd_i.

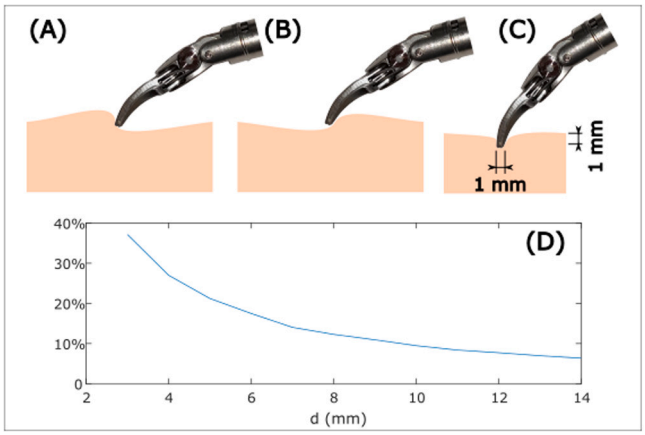

Fig. 5. Illustration of the measurement error caused by the uncertain contacting point on the VME.

Table 1
The suggested setting of d and Δd for improving the measurement accuracy.

	Displacement [mm]								
d	6	7	8	9	10	11	12	13	14
Δd	1	2	2	2	3	4	4	5	6

EBI sensor can tune to preserve a good sensing resolution. According to Eq. (5), the following Δd is proposed as shown in Table 1. Only integer is considered for d and Δd in this study. With this setting, the value of κ is within the range between 0.033 and 0.02. In total, VME is required to measure 13 positions on the tissue surface for each scanning according to Table 1.

3. Experimental evaluation

Three experiments were designed and performed for the evaluation of the proposed system and method. The first experiment was based on Finite Element Simulations (FES) for validation of the proposed concept. In addition, the impact due to the electrode' pressing depth on the tissue was also investigated. The second experiment was based on saline tank where different percentages of standard saline solutions were made and measured. To evaluate the measurement accuracy of the proposed system, the measured conductivity and permittivity using the proposed system was compared to the reference values. Subsequently, a more realistic experiment based on different ex vivo animal tissues was conducted. The third experiment aimed to demonstrate the use of the proposed system for real tissue measurement and classification. Reference values from previous studies were provided for comparison. The data processing and analysis was done using Matlab software and related toolbox (MathWorks Inc., MA, USA).

3.1. Finite element simulation

The FES experiment was carried out based on the AC/DC module of COMSOL Multiphysics software (COMSOL Inc., Sweden). As shown in Fig. 6, the MUT was modeled as a 200 mm × 100 mm × 100 mm block. Two electrodes in a similar shape as the instrument tip were drawn in the simulation representing the CSE and VME respectively. The material of the electrodes was set to be steel. Also, a relatively big area on the left side of the block was set as the electric ground. To simplify the simulation, we assumed that σ and ε of the MUT was 1 S/m and 1000 respectively, and independent from the frequency.

Normally, the pressing depth of CSE and VME into the tissue was difficult to control or measure accurately due to the soft tissue deformation. As described in Section 2.4, the electrode were controlled to push 2 mm on the tissue surface. The pressing on the tissue deformed the tissue and made it reshape around the electrode. This was equivalent to an immersed depth of electrodes h which should be smaller than 2 mm considering the tissue deformation. To study the impact of this parameter, different immersed depth for CSE and VME including 1 mm and 2 mm were implemented during the simulation. In addition, the amplitude of the excitation current is set to be 1 mA, and the frequency is set to be 100 kHz. Then the simulation measured the electrical potential of VME by running a parameter sweep with VME moving to the right in a displacement of d according to Table 1. After the voltages on VME were collected, the corresponding σ and ε_r were calculated.

3.2. Saline tank experiment

The saline tank experiment was designed to evaluate the measurement accuracy of the proposed system. Standard saline solutions including 0.1%, 0.2%, and 0.3% were made and used. These percentages of saline solutions were selected because they are within the range of most tissue types empirically [16]. A plastic container (200 mm × 130 mm × 75 mm) filled with saline solution was used as the saline tank (Fig. 7(A)). The left bottom corner of the saline tank was

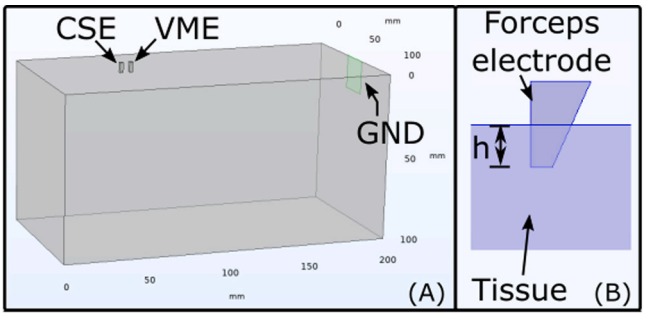

Fig. 6. (A) The setup of FES experiment for validating the proposed sensing method; (B) The electrode immersed depth h is considered as a variable during the simulation study.

placed to the origin of the global frame in the system setup. Also, a piece of copper tape (10 mm × 30 mm) was used as the GND electrode and was attached to the right wall of the saline tank.

During the experiments, the tip of CSE was controlled to the position X = 30 mm and Y = 65 mm. Then the VME was controlled by the robot arm to align with the CSE in Y axis and then move along the X+ direction in different d and Δd as described in Table 1. After the VME reached each target position, 100 measurements were collected continuously. Each measurement contained 30 data corresponding to the magnitude and phase angle at 15 frequencies.

In this experiment, the measurement accuracy due to different pressing depth was also investigated. The tips of both instruments were first adjusted to just contact the water surface, and then moved downwards a specific displacement. Two immersed depths h of 1 and 2 mm were tested. For each condition, the experiments were repeated 9 times. The calculated $\bar{\sigma}$ and $\bar{\varepsilon}_r$ were computed and compared to the reference values in Section 4.1.

3.3. Experiments with ex vivo animal tissues

The third experiment was designed to demonstrate the use of the proposed system on measuring bioimpedance spectroscopy on different biological tissues, and to evaluate the tissue classification based on the computed $\bar{\sigma}$ and $\bar{\varepsilon}_r$.

In total, five different tissues were prepared including porcine liver, porcine muscle, bovine muscle, chicken muscle and porcine fat. As a preliminary evaluation, the tissue samples were from wet market considering that the electrical property of a tissue types among mammals can be close [30]. The tissue samples were put in a plastic container (210 mm × 140 mm × 60 mm) and a copper plate was placed on the right side of the tissue sample as the GND electrode. During the experiments, the user selected a target position of which the tissue in the region is homogeneous and relatively far from the GND electrode. The RAEIS system then controlled the CSE to reach the target tissue surface and pressed 2 mm downwards. After the user inputted a scanning direction (X+ direction in this experiment), the RAEIS system controlled the VME to move along the defined direction for electric potential scanning with the optimized scanning displacements (Table 1) and required motion (Fig. 4). The measurements on each tissue sample were repeated 10 times. The values of $\bar{\sigma}$ and $\bar{\varepsilon}_r$ of each tissue type were computed.

Furthermore, a tissue classifier based on Support Vector Machine (SVM) was trained and tested on the collected data. The tissue classifications were performed to validate the feasibility of identifying different tissue types based on their electrical characteristics. Each input data was a vector consisting of 15 values of $\bar{\sigma}$ and 15 values of $\bar{\varepsilon}_r$, representing one impedance spectrum composed of 15 frequencies. The Classification Learner app of Matlab was used. Due to the small number of dataset, 2-fold cross-validation was implemented for computing the classification accuracy. To avoid overfitting, only linear kernel function was used.

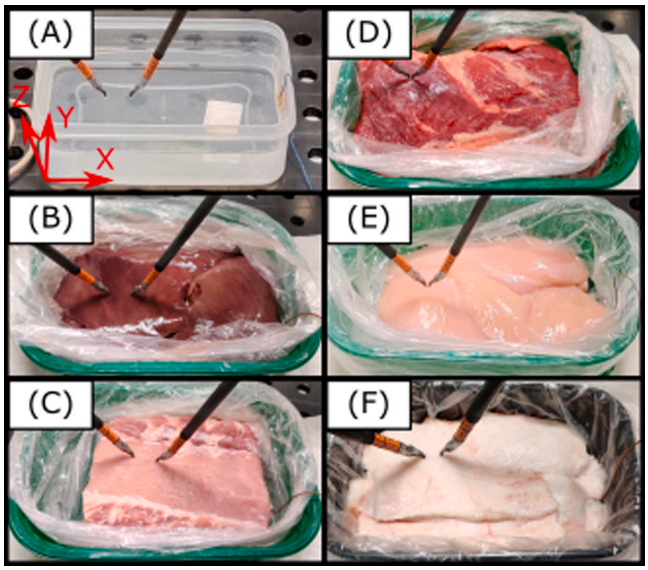

Fig. 7. The setup of the ex vivo experiment. Different phantoms and ex vivo tissues were used including (A) saline tank, (B) porcine liver, (C) porcine muscle, (D) bovine muscle, (E) chicken muscle, and (F) porcine fat.

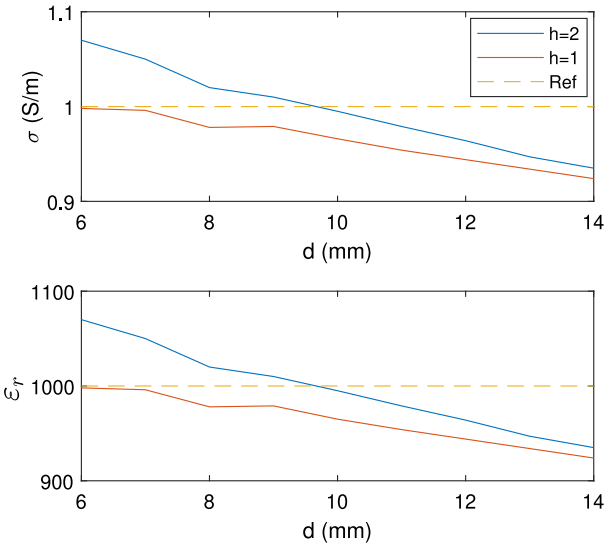

Fig. 8. The simulation results of σ and ε_r obtained at different d positions.

4. Results

4.1. Results of finite element simulation

The simulation results of σ and ε_r are presented against d as shown in Fig. 8. The σ value ranges from 1.07 to 0.94 S/m for condition h = 2 mm, and ranges from 1.0 to 0.92 S/m for condition h = 1 mm. As for the values of ε_r, the range is from 1071.3 to 935.2, and from 998.2 to 924.1 for the case of h = 2 mm and h = 1 mm respectively. In addition, we calculate the value of $\bar{\sigma}$ and $\bar{\varepsilon}_r$ based on Eqs. (9) and (10). The values of $\bar{\sigma}$ for h = 1 and 2 mm are found to be 0.97 S/m and 1 S/m respectively. The results of $\bar{\varepsilon}_r$ for immersed depth 1 and 2 mm are 970.2 and 1008.5 respectively. Given the ground truth of 1 S/m for the conductivity and 1000 for the permittivity, the simulation values indicate a considerably high accuracy.

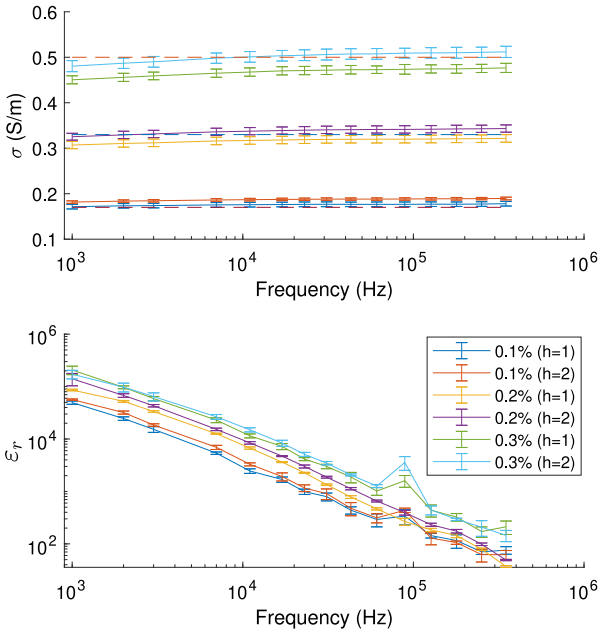

Fig. 9. The experimental results of the $\bar{\sigma}$ and $\bar{\varepsilon}_r$ values measured in 0.1%, 0.2% and 0.3% NaCl solutions and at 15 excitation frequencies.

4.2. Measurement results of different salines

The experimental results of saline tank are processed and presented in Fig. 9. For noise reduction, 100 data are measured at each d position, and a low pass filter is implemented by averaging the values. The measurements are repeated 5 times for each immersed depth and for each saline solution. In addition, the results of $\bar{\sigma}$ and $\bar{\varepsilon}_r$ are computed, and their mean and standard deviation at 15 frequencies are shown in Fig. 9. In the plot of $\bar{\sigma}$ values, the reference values according to IEC 60746-3 are also shown as dash lines. The $\bar{\sigma}$ values of the same saline solution are put together, and the RMSE with respect to the reference value are computed. The results indicate a very high accuracy given that the RMSE are 0.019 S/m, 0.224 S/m, and 0.447 S/m for 0.1%, 0.2% and 0.3% saline solutions respectively. With respect to the $\bar{\varepsilon}_r$ figure, no standard values can be found. Nevertheless, a similar trend and values are reported in study [31].

4.3. Experimental results of different ex vivo tissues

The experimental results ($\bar{\sigma}$ and $\bar{\varepsilon}_r$) of liver, muscle and fat are presented in Fig. 10, Fig. 11 and Fig. 12 respectively. In addition, reference values from previous studies are plotted for comparison [32–38]. The results of all three kinds of muscle samples are plotted in the same figure (Fig. 11) due to the consideration of similar tissue compositions.

The tissue classification results based on SVM achieved 100% accuracy, since there are significant differences of the electrical properties between liver, muscle and fat. Even among the muscle tissues from different animals, a simple linear kernel based SVM can successfully classify them with 100% accuracy.

The time used for the whole procedure is reported as follows. The RAEIS system takes about 8 s to perform the scanning of a point, and an average of 0.032 s to compute the results of $\bar{\sigma}$ and $\bar{\varepsilon}_r$.

5. Discussion

The experimental results demonstrate the capability and potential of the RAEIS system for measuring the electrical characteristics of biological tissues during RAMIS. A high measurement accuracy is observed

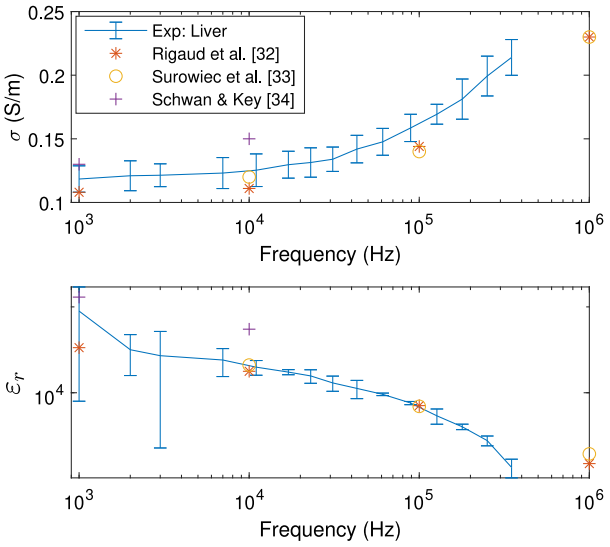

Fig. 10. The experimental results of liver samples based on the RAEIS system and the reference values from the other studies.

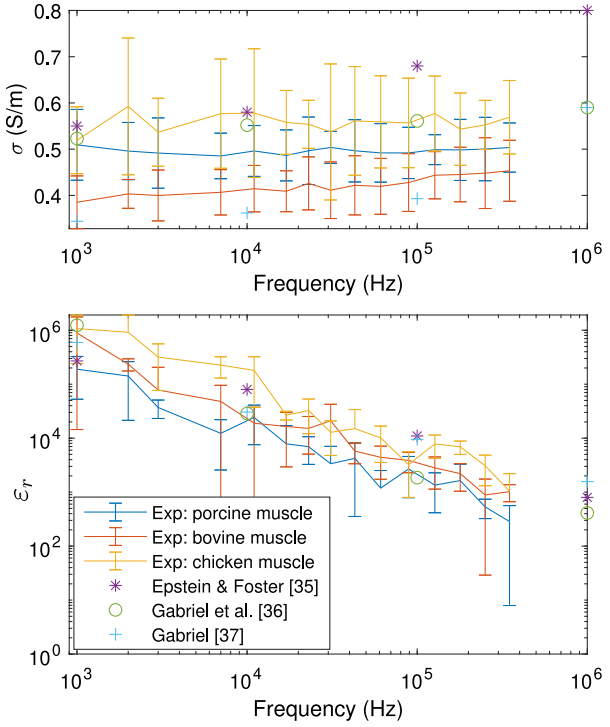

Fig. 11. The experimental results of three different muscle samples based on the RAEIS system and the reference values from the other studies.

according to the results of the FES experiment and the saline tank experiment. As shown in the simulation results, the values of σ and ε are within a reasonable range although a decreasing trend is observed. One possible reason is the electric field distortion since the GND is placed on one side of the phantom. Only one GND is used in this study to emulate the one current return pad commonly used in electrosurgery. In practice, it is possible to attach another GND pad on the other side of the patient for driving a more evenly distributed electric field. This study in particular focuses on the optimization of electrode positioning. Specifically, the range of d is controlled between 6 mm and 20 mm in order to minimize the error due to instrument' width and physiological noise. Also, different Δd_i for corresponding d_i are designed in order

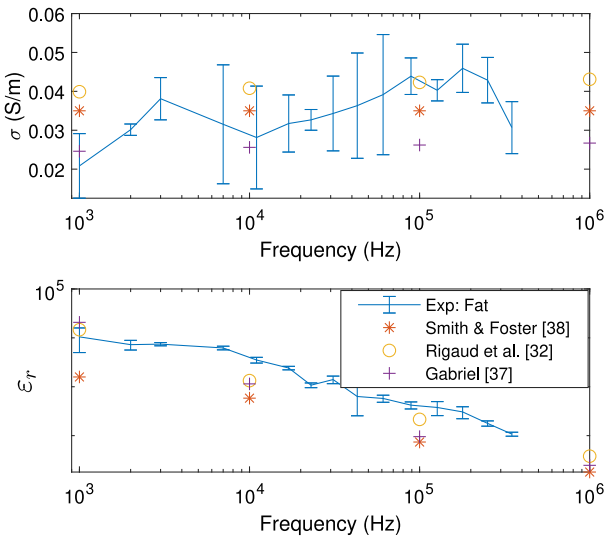

Fig. 12. The experimental results of fat samples based on the RAEIS system and the reference values from the other studies.

to keep κ consistent. In addition, Fig. 8 shows that there is a small variation of the results ($\leq 7\,\%$) due to the immersed depth h. This variation decreases significantly for a bigger d. All these variations can be successfully compensated by the weighted sum calculation given that the final results ($\bar{\sigma}$ and $\bar{\varepsilon}_r$) have $\leq 3\,\%$ error rate. In addition, the high sensing accuracy is also demonstrated by the small RMSE of the saline tank experiment (Fig. 9) under the conditions of different immersed depths. Compared to the variance due to parameter h, the differences of electrical characteristics between different tissue types and between healthy status and pathological status are generally much higher [37,39]. Thus, the proposed system and measurement method is suitable for the application of different tissues recognition.

Although the tri-polar sensing configuration exploited in the proposed RAEIS system can restrain the impact due to the electrodes pressing depth, the system requires a relatively high position accuracy (submillimeter level). This may be challenging to achieved directly based on the robot kinematic control for some existing robotic platform. Possible solution is to involve optical tracking facility or vision system for close loop position control [40]. The vision system can also reconstruct the tissue surface. By this means, the VME positions can be planned and guided in a 2D or 3D space during the scanning. This can further improve the system flexibility and prevent scanning in dirty or unreachable region. These aspects will be studied in future works and special focus will be on the system demonstration in a more relevant clinical environment.

According to the results of the ex vivo tissue experiment, the values of $\bar{\sigma}$ and $\bar{\varepsilon}_r$ are found to be consistent given that the standard deviations of the results are generally small. The RAEIS system enables the estimation of material's conductivity and relative permittivity, rather than a complex impedance value which is dependent on the electrode configuration. In this case, the sensing results can be easily reused and compared to the ones available in literature. In fact, the obtained values of different tissue types are found close to the results presented in the other researches, which are based on more controlled acquisition conditions such as using custom designed probes. In addition, the results show that the conductivity and permittivity of biological materials are frequency-dependent, which have been also reported in previous studies [30]. Specifically, with the increase of excitation frequency, tissues generally become more conductive, while its permittivity becomes smaller. As interpreted in [41], the impedance at low frequencies gives information about the cell volume fraction since isolating cell membranes decreases the current path. When high frequency excitation signal is used, more information related to the intra-cellular component is involved. These characteristics support the improved identification of different tissue types by using a wide-band spectroscopic information. The strong tissue identification capability of the proposed system is confirmed by the classification results, where a 100% accuracy is obtained for the 5 considered tissue types. Even for the same type of tissues (i.e., muscle) from different animals, the slightly different tissue compositions can be reflected by their electrical properties. Nevertheless, future work is needed to optimize the number and range of the excitation frequencies in order to assure a high tissue recognition accuracy in more complicated and realistic surgical scenario.

While these findings are encouraging, the evaluation experiments in this study is preliminary. Given that the intra-sample variance is much smaller compared to the differences between different tissue types, the tissue recognition task could be achievable. Nevertheless, several factors can impact the tissues' electrical property such as temperature, moisture, and age. Therefore, repeating sampling and on different locations and use different samples of the same types are undertaken to ensure the accurate of the conclusion. Furthermore, as pointed out by many previous researches, the electrical property of tissue can have significant change when it becomes pathological [16]. This implies a great potential for the RAEIS system to offer pathological tissue detection intra-operatively. Also, in vivo human tissues can be different in an absolute sense from the ex vivo animal tissues shown in this study. Given that mammal tissues have similar electrical property [36,37], ex vivo animal tissues are used for preliminary evaluation. These results allow us to extend this research to more realistic and meaningful experiments on in vivo animal or human for future evaluation. Another interesting future research can be on the sensing of heterogeneous material which may happen on tumor margin. particularly, future experiment will involve the consideration of blood and body fluid on the tissue surface and other physiological signals which can potentially increase the noise level of the measurement. For this, the sensitivity optimization through electrode position arrangement and weight setting design in Eq. (11) may be useful. In addition, more advanced machine learning based algorithm will be investigated for ensuring an accurate tissue classification [18].

In the proposed RAEIS system the distal tip of the scissors is used as an electrode and the internal electrical connections are used for connecting the spectroscopic device. This solution, combined with the accurate control of immersed depth of the instrument tip in the tissue, can be modeled as a small electrode in the sensing configuration. By this means, no modifications to the standard surgical instrument are required, allowing this approach to be easily extended to any electrified instrument. Also, thanks to its flexibility, the RAEIS technique can complement the other existing sensing modalities, and sensor fusion technique can be implemented for enhanced accuracy. In practice, an electric switch or relay can be connected to the electric end of the instrument for switching the electrocautery function and the EBI measurement. Through the RAEIS system, the surgeon can obtain the electrical characteristics of a suspicious region and compare the measured values to the values acquired in a certainly healthy region or to a pre-defined database. This information can be displayed by means of Augmented Reality in the user console [25] or integrated to the decision making strategy of the future autonomous surgical robot [4]. Especially for novice surgeon, tissue classification and labeling can be beneficial to the confidence level in surgical decision and context awareness.

6. Conclusion

In this study, we present the system and algorithms development for tissue inspection or identification during a RAMIS. The proposed system utilizes a tri-polar sensing configuration which can be realized by incorporating 2 robotic instruments. Without involving external

sensing probes to the operation site, the proposed method can be easily applied in most commercial surgical robotic platforms and enhances the perception capability in an accurate, cost-effective and safe manner. Since the robotic control provides flexible electrode placement, the electrode position is optimized for improving the signal noise ratio. Experiments on ex vivo demonstrate that the system is able to perform autonomous scanning on a target tissue region and computes the electrical conductivity and permittivity of tissue in multiple spectrum. Based on the tissue electrical characteristics, classifier is developed to identify different tissue types, which can be further extended to indicate tissue's health status on site and in real time.

CRediT authorship contribution statement

Zhuoqi Cheng: Conceptualization, Methodology, Software, Investigation, Writing – original draft, Writing – review & editing, Visualization. **Diego Dall'Alba:** Conceptualization, Methodology, Writing – original draft, Writing – review & editing. **Kim Lindberg Schwaner:** Software, Investigation, Writing – review & editing, Visualization. **Paolo Fiorini:** Writing – review & editing, Project administration, Funding acquisition, Supervision. **Thiusius Rajeeth Savarimuthu:** Writing – review & editing, Project administration, Funding acquisition, Supervision.

Declaration of competing interest

The authors declare that they have no known competing financial interests or personal relationships that could have appeared to influence the work reported in this paper.

Acknowledgments

This project has received funding from the European Research Council (ERC) under the European Union's Horizon 2020 research and innovation programme (grant agreement No. 742671 – ARS).

References

[1] V. Vitiello, K.-W. Kwok, G.-Z. Yang, Introduction to robot-assisted minimally invasive surgery (MIS), in: Medical Robotics, Elsevier, 2012, pp. 1–P1.
[2] G. Dogangil, B. Davies, F. Rodriguez y Baena, A review of medical robotics for minimally invasive soft tissue surgery, Proc. Inst. Mech. Eng. H 224 (5) (2010) 653–679.
[3] Intuitive Surgical, Inc., Intuitive surgical annual report, 2020, URL https://isrg.intuitive.com/static-files/80b10bf5-c1da-4ad3-bb0e-8c595e2c712c.
[4] A. Attanasio, B. Scaglioni, E. De Momi, P. Fiorini, P. Valdastri, Autonomy in surgical robotics, Annu. Rev. Control Robot. Auton. Syst. 4 (2020).
[5] R. Muradore, P. Fiorini, G. Akgun, D.E. Barkana, M. Bonfe, F. Boriero, A. Caprara, G. De Rossi, R. Dodi, O.J. Elle, et al., Development of a cognitive robotic system for simple surgical tasks, Int. J. Adv. Robot. Syst. 12 (4) (2015) 37.
[6] Z. Cheng, T.R. Savarimuthu, A novel robot assisted electrical impedance scanning system for subsurface object detection, Meas. Sci. Technol. (2021).
[7] Z. Cheng, K.L. Schwaner, D. Dall'Alba, P. Fiorini, T.R. Savarimuthu, An electrical bioimpedance scanning system for subsurface tissue detection in robot assisted minimally invasive surgery, IEEE Trans. Biomed. Eng. 69 (1) (2022) 209–219.
[8] A.M. Okamura, Haptics in robot-assisted minimally invasive surgery, in: The Encyclopedia of MEDICAL ROBOTICS: Volume 1 Minimally Invasive Surgical Robotics, World Scientific, 2019, pp. 317–339.
[9] E. Vander Poorten, E. Demeester, P. Lammertse, Haptic feedback for medical applications, a survey, in: Proceedings Actuator 2012, 2012.
[10] U. Kim, D.-H. Lee, W.J. Yoon, B. Hannaford, H.R. Choi, Force sensor integrated surgical forceps for minimally invasive robotic surgery, IEEE Trans. Robot. 31 (5) (2015) 1214–1224.
[11] A. Faragasso, A. Stilli, J.a. Bimbo, H.A. Wurdemann, K. Althoefer, Multi-axis stiffness sensing device for medical palpation, in: 2015 IEEE/RSJ International Conference on Intelligent Robots and Systems, IROS, IEEE, 2015, pp. 2711–2716.
[12] A. Garg, S. Sen, R. Kapadia, Y. Jen, S. McKinley, L. Miller, K. Goldberg, Tumor localization using automated palpation with gaussian process adaptive sampling, in: 2016 IEEE International Conference on Automation Science and Engineering, CASE, IEEE, 2016, pp. 194–200.
[13] Y. Sun, W. Wang, Q. Zhang, X. Zhao, L. Xu, H. Guo, Intraoperative ultrasound: technique and clinical experience in robotic-assisted renal partial nephrectomy for endophytic renal tumors, Int. Urol. Nephrol. 53 (3) (2021) 455–463.
[14] O.G. Martinsen, S. Grimnes, Bioimpedance and Bioelectricity Basics, Academic Press, 2011.
[15] Z. Cheng, B.L. Davies, D.G. Caldwell, L.S. Mattos, A new venous entry detection method based on electrical bio-impedance sensing, Ann. Biomed. Eng. 46 (10) (2018).
[16] Z. Cheng, A.L.C. Carobbio, L. Soggiu, M. Migliorini, L. Guastini, F. Mora, M. Fragale, A. Ascoli, S. Africano, D. Caldwell, et al., SmartProbe: a bioimpedance sensing system for head and neck cancer tissue detection, Physiol. Meas. (2020).
[17] E.K. Murphy, A. Mahara, S. Khan, E.S. Hyams, A.R. Schned, J. Pettus, R.J. Halter, Comparative study of separation between ex vivo prostatic malignant and benign tissue using electrical impedance spectroscopy and electrical impedance tomography, Physiol. Meas. 38 (6) (2017) 1242.
[18] B. Kent, C. Rossa, Electric impedance spectroscopy feature extraction for tissue classification with electrode embedded surgical needles through a modified forward stepwise method, Comput. Biol. Med. 135 (2021) 104522.
[19] R.J. Halter, A. Schned, J. Heaney, A. Hartov, K.D. Paulsen, Electrical properties of prostatic tissues: II. Spectral admittivity properties, J. Urol. 182 (4) (2009) 1608–1613.
[20] A. Pathiraja, P. Ziprin, A. Shiraz, R. Mirnezami, A. Tizzard, B. Brown, A. Demosthenous, R. Bayford, Detecting colorectal cancer using electrical impedance spectroscopy: an ex vivo feasibility study, Physiol. Meas. 38 (6) (2017) 1278.
[21] J. Yun, Y.-T. Hong, K.-H. Hong, J.-H. Lee, Ex vivo identification of thyroid cancer tissue using electrical impedance spectroscopy on a needle, Sensors Actuators B 261 (2018) 537–544.
[22] G. Zhu, L. Zhou, S. Wang, P. Lin, J. Guo, S. Cai, X. Xiong, X. Jiang, Z. Cheng, Design of a drop-in EBI sensor probe for abnormal tissue detection in minimally invasive surgery, J. Electr. Bioimpedance 11 (1) (2020) 87.
[23] V. Cherepenin, A. Karpov, A. Korjenevsky, V. Kornienko, D. Meister, A 3D electrical impedance tomography (EIT) system for breast cancer detection, Physiol. Meas. 22 (1) (2001) 9–18.
[24] H. Tan, C. Rossa, Electrical impedance tomography for robot-aided internal radiation therapy, Front. Bioeng. Biotechnol. 9 (2021).
[25] Z. Cheng, D. Dall'Alba, S. Foti, A. Mariani, T. Chupin, D.G. Caldwell, G. Ferrigno, E. De Momi, L.S. Mattos, P. Fiorini, Design and integration of electrical bioimpedance sensing in surgical robotic tools for tissue identification and display, Front. Robot. AI 6 (2019) 55.
[26] K.S. Cole, R.H. Cole, Dispersion and absorption in dielectrics I. Alternating current characteristics, J. Chem. Phys. 9 (4) (1941) 341–351.
[27] M. Amini, J. Hisdal, H. Kalvøy, Applications of bioimpedance measurement techniques in tissue engineering, J. Electr. Bioimpedance 9 (1) (2018) 142–158.
[28] Z. Cheng, D. Dall'Alba, D.G. Caldwell, P. Fiorini, L.S. Mattos, Design and integration of electrical bio-impedance sensing in a bipolar forceps for soft tissue identification: A feasibility study, in: International Conference on Electrical Bioimpedance, Springer, 2019, pp. 3–10.
[29] U. Pliquett, D. Frense, M. Schönfeldt, C. Frätzer, Y. Zhang, B. Cahill, M. Metzen, A. Barthel, T. Nacke, D. Beckmann, Testing miniaturized electrodes for impedance measurements within the β-dispersion–a practical approach, J. Electr. Bioimpedance 1 (1) (2019) 41–55.
[30] D. Andreuccetti, An internet resource for the calculation of the dielectric properties of body tissues in the frequency range 10 Hz-100 GHz, 2012, http://niremf.ifac.cnr.it/tissprop/.
[31] L.F. Lima, A.L. Vieira, H. Mukai, C.M. Andrade, P.R. Fernandes, Electric impedance of aqueous KCl and NaCl solutions: Salt concentration dependence on components of the equivalent electric circuit, J. Molecular Liquids 241 (2017) 530–539.
[32] B. Rigaud, L. Hamzaoui, N. Chauveau, M. Granie, J.-P.S. Di Rinaldi, J.-P. Morucci, Tissue characterization by impedance: a multifrequency approach, Physiol. Meas. 15 (2A) (1994) A13.
[33] A. Surowiec, S. Stuchly, L. Eidus, A. Swarup, In vitro dielectric properties of human tissues at radiofrequencies, Phys. Med. Biol. 32 (5) (1987) 615.
[34] H.P. Schwan, C.F. Kay, Capacitive properties of body tissues, Circ. Res. 5 (4) (1957) 439–443.
[35] B. Epstein, K. Foster, Anisotropy in the dielectric properties of skeletal muscle, Med. Biol. Eng. Comput. 21 (1) (1983) 51–55.
[36] S. Gabriel, R. Lau, C. Gabriel, The dielectric properties of biological tissues: II. Measurements in the frequency range 10 Hz to 20 GHz, Phys. Med. Biol. 41 (11) (1996) 2251.
[37] C. Gabriel, Compilation of the Dielectric Properties of Body Tissues at RF and Microwave Frequencies, Tech. Rep., King's Coll London (United Kingdom) Dept of Physics, 1996.
[38] S.R. Smith, K.R. Foster, Dielectric properties of low-water-content tissues, Phys. Med. Biol. 30 (9) (1985) 965.
[39] H. Wang, Y. He, M. Yang, Q. Yan, F. You, F. Fu, T. Wang, X. Huo, X. Dong, X. Shi, Dielectric properties of human liver from 10Hz to 100MHz: normal liver, hepatocellular carcinoma, hepatic fibrosis and liver hemangioma, Biomed. Mater. Eng. 24 (6) (2014) 2725–2732.
[40] V. Penza, Z. Cheng, M. Koskinopoulou, A. Acemoglu, D.G. Caldwell, L.S. Mattos, Vision-guided autonomous robotic electrical bio-impedance scanning system for abnormal tissue detection, IEEE Trans. Med. Robot. Bionics 3 (4) (2021) 866–877.
[41] S. Grimnes, O.G. Martinsen, Bioimpedance and Bioelectricity Basics, Academic Press, 2011.